Impulse-driven oscillations of the near-Earth's magnetosphere

Hiroatsu Sato[1], Hans L. Pécseli[2,4], Jan K. Trulsen[3], Per Even Sandholt[4], and Charles J. Farrugia[5]

[1]DLR Institute for Solar-Terrestrial Physics, D-17235 Neustrelitz, Germany
[2]Department of Physics and Technology, Arctic University of Norway, N-9037 Tromsø, Norway
[3]Institute of Theoretical Astrophysics, University of Oslo, Boks 1048 Blindern, N-0316 Oslo, Norway
[4]Department of Physics, University of Oslo, Boks 1029 Blindern, N-0315 Oslo, Norway
[5]Institute for the Study of Earth, Oceans, and Space, Morse Hall, University of New Hampshire, 8 College Road, Durham, NH, USA

Correspondence: Hans L. Pécseli (hans.pecseli@fys.uio.no)

Abstract. It is argued that a simple model based on magnetic image arguments suffices to give a convincing insight into both the basic static as well as dynamic properties of the near-Earth's magnetosphere. Qualitative results can be obtained for the heating due to the compression of the radiation belts. The properties of this simple dynamic model for the solar wind – magnetosphere interaction are discussed and compared to observations. In spite of its simplicity, the model gives convincing

5 results concerning the magnitudes of the near-Earth's magnetic and electric fields. The database contains ground based results for magnetic field variation in response to shocks in the solar wind. The observations also include satellite data, here from the two Van Allen satellites.

1 Introduction

Instrumented spacecraft in the near-Earth's magnetosphere detect significant dynamic variations in the magnetic fields and

10 plasma properties in response to variations in the solar wind (*Araki*, 1994; *Archer et al.*, 2013). The abrupt increase in pressure associated with interplanetary shocks driven, for instance, by interplanetary coronal mass-ejections (ICME) will compress the low-latitude geomagnetic field through an intensification of the Chapman-Ferraro magnetopause current. This leads to a sudden impulse (SI) which can be observed also in low-latitude magnetometer records. It was demonstrated (*Farrugia and Gratton*, 2011) that such SI-events are often followed by oscillations of ~ 5 min periods. These can be observed also by satellites in the

15 cold, dense magnetosheath and the hot and tenuous magnetospheric plasmas, consistent with also other related observations (*Plaschke et al.*, 2009). The presence of magnetic pulsations with periods 8-10 min measured by geosynchronous satellites are found to be well correlated with variations in the solar wind dynamic pressure (*Kivelson et al.*, 1984; *Sibeck et al.*, 1989; *Korotova and Sibeck*, 1995).

A simple dynamic model for the solar wind – magnetosphere interaction was proposed by *Børve et al.* (2011). In its simplest

20 version, the model uses a plane interface between the Earth's magnetic dipole field and an ideally conducting solar wind. This approach has an exact analytical solution in terms of an image method (*Stratton*, 1941; *Alfvén*, 1950). While the model has tutorial value it is not clear to what extent it can be used for predictions of parameter variations of the magnetospheric oscillations and overall changes of the magnetosphere in response to abrupt changes in the solar wind. The present study

addresses this question using data from space observations obtained using in situ data acquired by spacecraft and also ground
25   based observations.
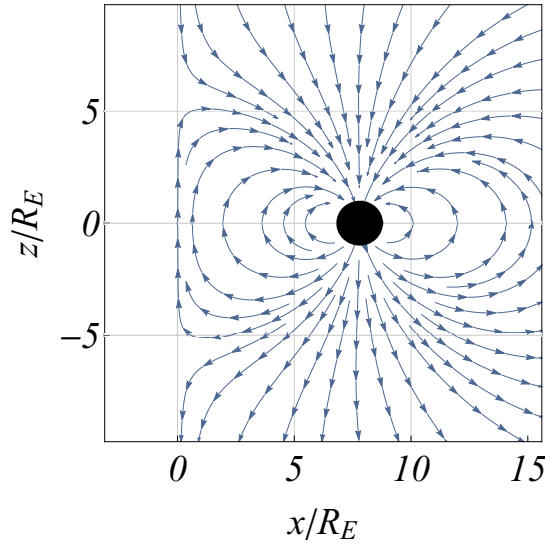
Figure 1. *Illustration of a cut in a model magnetosphere assuming a plane interface between the Earth's magnetic dipole field and an ideally conducting solar wind. Distances are normalized by the radius of the Earth, R_E. The sun is in the negative x-direction. The stagnation point of the solar wind is here at the position $(x,z) = (0,0)$. The case illustrated here assumes a strong compression of the magnetosphere by a solar wind pressure pulse by taking the distance to the magnetopause to be 7.8 R_E. This value has relevance for data to be shown later. Note the formation of two cusp-points.*

As the impulse from an ICME-shock event arrives at the vicinity of the stagnation point of the solar wind at the magnetopause its perturbation propagates along the magnetosphere with velocity depending on the direction with respect to the magnetic field or the magnetopause. As an order of magnitude we can use

$$\vartheta = \frac{V_A}{\sqrt{1 + (V_A/c)^2}}$$

where $V_A = B/\sqrt{\mu_0 \rho}$ is the Alfvén speed and c the speed of light in vacuum. For vacuum or dilute plasmas we have $\vartheta \approx c$, for dense plasmas $\vartheta \approx V_A$. We assume the velocity ϑ to be sufficiently large to allow the motion of the magnetopause at all relevant points to be assumed instantaneous for the present problem.

2   A simple model

30   In its original form, the basic model (*Børve et al.*, 2011) assumed a plane interface between the solar wind and the near-Earth's magnetosphere. An equilibrium state is found when the solar wind ram pressure balances the magnetic field pressure at the stagnation point of the solar wind flow. The solar wind gives up all its parallel momentum as in an inelastic collision and flows
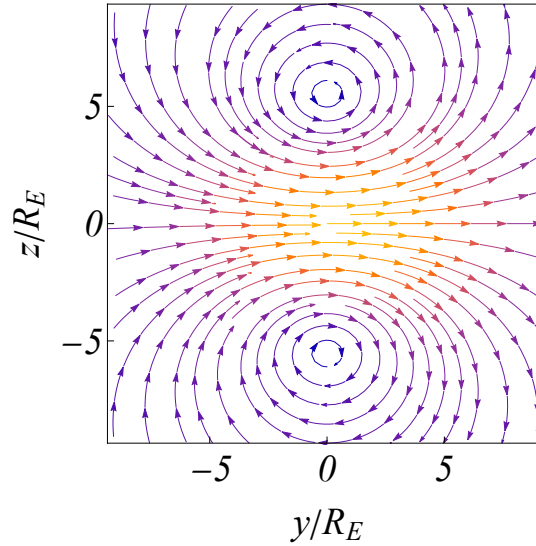
Figure 2. *The surface current on the interface between the near-Earth's magnetosphere and the solar wind, consistent with Fig. 1. Note the current loops circling the two cusp points.*

with a reduced velocity along the interface, i.e. the magnetopause, in a boundary layer with an otherwise unspecified thickness and plasma density. The model predicts static parameters such as the distance between the Earth and the magnetopause (stand-
35 off distance), as well as some dynamic features, in particular the frequency of magnetospheric oscillation in response to an impulsive perturbation in the solar wind. For describing the Earth's magnetic field we here ignore the small tilt of the magnetic axis with respect to the rotation axis. For generalizing the model to other planets it is straightforward to include such a tilt of the magnetic axis (*Børve et al.*, 2011).

2.1 Static limit

40 For this formulation the total magnetic field resulting from the Earth's dipole and the Chapman-Ferraro current can be found by a simple method of images with details as well as figures presented by *Børve et al.* (2011). The spatial variations of the magnetic field in the near-Earth's magnetosphere predicted by the model are illustrated here in Fig. 1. In particular, the model predicts the distance from the Earth to the stagnation point of the solar wind. The analysis can be generalized to account also for the curvature of the magnetosheath in the vicinity of the stagnation point, see Appendix A. The surface currents consistent
45 with Fig. 1 are shown in Fig. 2.

The equilibrium position R for the distance from the Earth to the magnetopause is found (*Børve et al.*, 2011) by equating the magnetic field pressure from the Earth's dipole moment Q_E to the solar wind ram pressure to give the relation

$$R = \left(\frac{\mu_0 Q_E^2}{8\pi^2 U^2 n \overline{M}} \right)^{1/6}, \tag{1}$$

with $n\overline{M}$, being the mass density of the solar wind in terms of density n and average ion mass $\overline{M}$. A numerical coeffi-
50   cient is here a result of the analysis and not a free adjustable parameter. Expressions similar to (1) can be found in the lit-
erature (*Walker and Russell*, 1995). The scaling with the solar wind dynamic pressure $\left(n\overline{M}U^2\right)^{-1/6}$ is generally accepted
(*Southwood and Kivelson*, 1990). In fact, apart from a numerical factor, it can be derived from basic dimensional reasoning as
shown in Appendix B. The predictions of the model for the distance from the Earth to the magnetopause are shown in Fig. 3
for later reference.
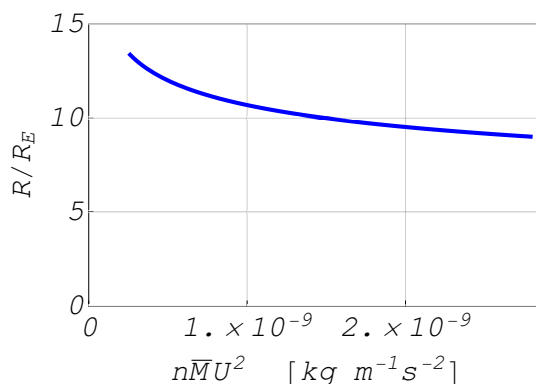
Figure 3. *Model predictions for the distance from the Earth to the magnetopause. The distance is measured in units of the Earth radius R_E
shown for varying momentum flux density $n\overline{M}U^2$ in the solar wind.*

55   The surface current that models the Chapman-Ferraro current at the interface between the Earth's magnetosphere and the
solar wind at $x = 0$ in Fig. 1 induces a small correction to the magnetic field at the surface of the Earth. A change of the
stand-off-distance R in Fig. 3 will give rise to a change in this correction as illustrated in Fig. 4. The illustration assumes a
change from a distance of $11\,R_E$ to a new steady state at $7.8\,R_E$. The three spheres show: the absolute value of the change in
magnetic field, the absolute value of the change in the horizontal magnetic field component, and finally the change in the
60   normal component with respect to the Earth surface. The latter case is shown including its sign, using the right hand side of the
color-bar. Following the standard convention we have positive values of the vertical magnetic field component B_v pointing into
the Earth. The two other cases have units to the left of the color bar. We use this example also to illustrate the consequences of a
tilt of the magnetic dipole axis, see Fig. 5. For cases relevant for the Earth we find this modification to be of little consequence,
and it is ignored in the following.

2.2 Dynamic features

In response to an impulse change in the solar wind ram pressure, the near-Earth's magnetosphere is set into motion. The
model of *Børve et al.* (2011) accounts for this by moving the image dipole in the simple plane interface model as well as in its
generalization summarized in the Appendix.
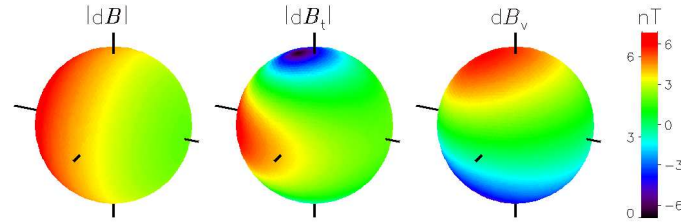
Figure 4. *Illustration of the change in the magnetic field, d$\mathbf{B}$, in nT at the surface of the Earth in response to a change in the distance between the Chapman-Ferraro current and the Earth. In this case the magnetopause moves from a distance of $11\,R_E$ to $7.8\,R_E$. The sun is to the left with the direction given by a small pointer, used also to give the north-south and east-west directions. The direction of the vertical magnetic field component is positive into the Earth. The 3 figures show $|d\mathbf{B}|$, the absolute value of the tangential component $|d\mathbf{B}_t|$ (left side of the color code), and the vertical component $d\mathbf{B}_V$ (right hand side of the color code), respectively. The change in $d\mathbf{B}_V$ is largest near the magnetic poles.*
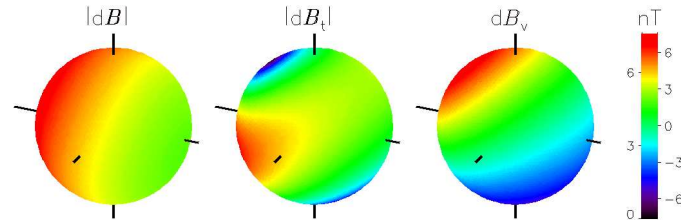
Figure 5. *Illustration of the consequences of a tilt of the magnetic dipole axis, here $15°$ in comparison to Fig. 4 where the magnetic dipole axis is vertical. The explanation of symbols is the same for these two figures.*

To find oscillating features a physical system needs inertia or its equivalent *Freeman et al.* (1995). The model is not able to predict this inertia, and it is here quantified by a thickness D and a mass density ρ which has to be determined by observations (*Song et al.*, 1990) or numerical simulations that are also available (*Spreiter et al.*, 1966). To discuss a finite amplitude nonlinear case, we write Newton's second law for the position of the interface in the form

$$D\rho\frac{d^2}{dt^2}\Delta = n\overline{M}\left(U - \frac{d\Delta}{dt}\right)^2 - 2\frac{\mu_0 Q_E^2}{(4\pi(R-\Delta)^3)^2}, \tag{2}$$

where $\Delta(t)$ is the time varying displacement of the interface from its equilibrium value R from (1). We take the sign-convention so that $\Delta > 0$ when the magnetopause boundary moves in the direction of the Earth (this definition differs from the one used by *Børve et al.* (2011)). The solar wind dynamic pressure in the first term of (2), is expressed in terms of the relative velocity between the solar wind and the moving magnetopause. The equilibrium solution of (2) with $\Delta = 0$ gives (1).

If we linearize (2) we can derive a characteristic oscillation period as

$$T_0 = \frac{2\pi}{\Omega} = 2\pi \sqrt{\frac{4\pi^2 R^7 D\rho}{3\mu_0 Q^2}} = 2\pi \frac{R}{U} \sqrt{\frac{D\rho}{6n\overline{M}R}}, \tag{3}$$

80 A damping coefficient can be found as $\sqrt{n\overline{M}U/D\rho}$. Large inertia ρD gives a long oscillation period and a reduced damping.
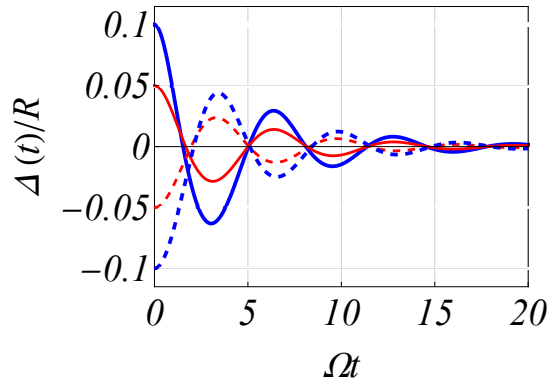
Figure 6. *Numerical solutions of the nonlinear normalized equation (4) for 4 pulse-like initial conditions, $\Delta(0)$, two positive corresponding to a compression, and two negative corresponding to rarefaction. Note that the figure is asymmetric with respect to the $\Delta = 0$ axis.*
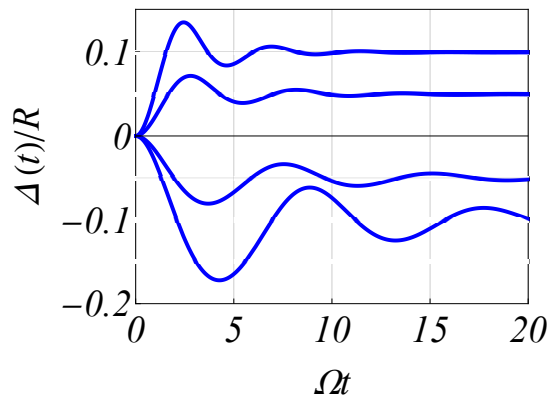
Figure 7. *Numerical solutions of the normalized equation (4). For $\Delta > 0$ the solution corresponds to a compression of the magnetosphere in response to a sudden step-like impulse, while $\Delta < 0$ corresponds to a sudden expansion.*

A relevant problem to be analyzed by (2) corresponds to a sudden pulse-like change in the solar wind plasma density, which we here model by changing $n\overline{M}$ while keeping U constant. The basic dynamic equation (2) can be rewritten in normalized

form (*Børve et al.*, 2011) as

$$
\begin{aligned}
\frac{d^2}{d\tau^2}Z &= \frac{1}{6}\left(1 - \frac{1}{(1-Z)^6}\right) \\
&\quad - \frac{2}{\sqrt{6}}\sqrt{\frac{RnM}{D\rho}}\frac{dZ}{d\tau} + \frac{RnM}{D\rho}\left(\frac{dZ}{d\tau}\right)^2 \\
&= -\frac{1}{6}\frac{1}{(1-Z)^6} + \frac{1}{6}\left(1 - \sqrt{\frac{6RnM}{D\rho}}\frac{dZ}{d\tau}\right)^2,
\end{aligned}
\tag{4}
$$

with $Z \equiv \Delta/R$ where R is the equilibrium solution (1), while time is normalized by T_0 from (3). The basic equation (4) is strongly nonlinear and the solutions are characterized by significant harmonic generation. The basic equation (4) can be solved for different conditions, the standard one being where Z is slightly displaced from the equilibrium position to perform damped oscillations, eventually reaching $Z = 0$ as illustrated in Fig. 6. Alternatively, as shown in Fig. 7, we can assume the interface at its equilibrium position until a reference time $\tau = 0$, where there is a sudden lasting change in the solar wind conditions, changing the equilibrium position. The differential equation has to be modified slightly to include this case (*Børve et al.*, 2011). For the large perturbations in Fig. 7 we find a typical velocity of the magnetosphere boundary taking a change in position $\Delta/R \approx 0.05$ within a time $T_0/5$, to give the velocity $\Delta/T_0 \approx 0.25 R/T_0$.

The reference calculations in Fig. 7 use $Rn\overline{M} = D\rho/4$, i.e. a relatively large inertia associated with the moving magnetopause. To illustrate the nonlinear character of the oscillations, we show solutions for both positive and negative changes in the solar wind momentum density. For a linear system, the positive and negative parts of Fig. 7 should be mirror images with respect to the horizontal axis. We expect, however, generally a different nonlinear response to a sudden increase and a sudden rarefaction in the solar wind. Also this may occur, albeit not as often as compression by a shock. It is found that the term containing $(dZ/d\tau)^2$ reduces the damping slightly for realistic amplitudes. Details of the derivation of the results summarized here are given by *Børve et al.* (2011), in particular also discussing the simplified linearized limit of the equations.

The physical mechanism causing the damping is found to be a phase-lag between the forcing and the displacement of the magnetospheric boundary when the fact that the momentum transfer depends on the solar wind velocity relative to the moving boundary is taken into account. The damping is not due to dissipation. A somewhat similar result was found by *Chen and Hasegawa* (1974), studying a related problem.

The motion of the Chapman-Ferraro current system induces temporal variations in the magnetic field detected at the surface of the Earth. These are illustrated in Fig. 8. The asymptotic limits $t \to \infty$ correspond to Figs. 4 and 5. The analytical expression for the B-field perturbation at the magnetic equator as found by use of the image dipole is

$$
\begin{aligned}
dB(t) = \quad &\frac{\mu_0 Q_E}{4\pi R^3}\left(\frac{1}{(1 - \Delta(t)/R - R_E/2R)^3}\right. \\
&\left. - \frac{1}{(1 - R_E/2R)^3}\right).
\end{aligned}
\tag{5}
$$

The nonlinear features of $\Delta(t)$ are magnified by the analytical form of dB_θ, the oscillation period depending, in particular, on the sign and perturbation amplitude. In Fig. 8 we introduced the normalizing by B_{R_E} being the B-field at magnetic equator
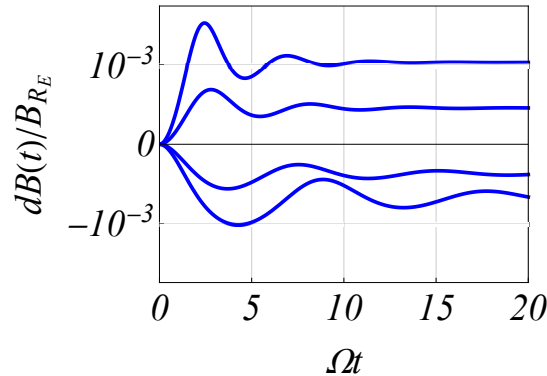
Figure 8. *Numerical solutions of the normalized equation (4) used for calculating the variations in the magnetic field as detected at magnetic equator on Earth. The curves correspond to those in Fig. 7. The figure uses $R_E/R = 0.13$.*

at $t = 0$; we have a representative value of $B_{R_E} = 30 \ \mu T$. A characteristic value for the perturbation of the magnetic field deduced from Fig. 8 is thus $dB \approx 30 \ nT$ for the given parameters.

The time-varying model magnetic field has a straightforward analytical expression in terms of the moving image dipole. By Faraday's law (or by $\mathbf{E} = \mathbf{U} \times \mathbf{B}$) the induced electric field can be derived, as illustrated here in Fig. 9 for the case where the Chapman-Ferraro current system moves with constant velocity. This is here modeled by moving the image magnetic dipole. Note that a calculation starting from the moving Chapman-Ferraro current system would be complicated, while the result from a moving image dipole is simple. Oscillations in Δ seen in Figs. 6 and 7 give corresponding time variations in the magnetic field. A change in the sign of $\partial \mathbf{B}/\partial t$ gives rise to a corresponding change in the sign of the induced electric field in Fig. 9.

The discussion so far assumed that the density of matter, plasma in particular, is negligible between the Earth and the magnetopause. We discuss next the effects on the radiation belts and the Earth's near ionosphere.

2.2.1 Motions of the radiation belts.

The moving Chapman-Ferraro current system induces $\mathbf{E} \times \mathbf{B}/B^2$-motions of the radiation belts as illustrated in Fig. 10, there shown in the horizontal plane of Fig. 9. In the analysis we assumed initially quiet conditions with the stagnation point at a large distance from the Earth, see Fig. 1, so that the boundary of the radiation belts can be assumed circular. The moving Chapman-Ferraro current system is then allowed to move the stagnation point from $11R_E$ to a distance of $7.8R_E$ from the Earth. We note that the inner boundary is hardly affected since the Earth's magnetic field is too strong there. The deformation of the outer boundary is asymmetric: at the magneto-tail side the electric fields are too weak to induce a motion of any significance, see Fig. 9. The outer boundary on the sun-ward side, is on the other hand compressed because the magnetic field is relatively weak while the induced electric field have a sufficient magnitude to give a noticeable $\mathbf{E} \times \mathbf{B}/B^2$-motion. It turns out that the velocity of the compression does not matter: only the initial and final positions of the magnetopause matter. The conclusion is
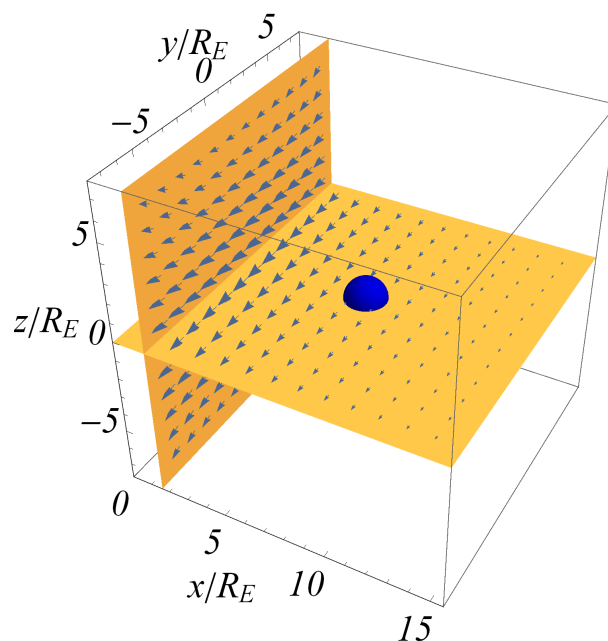
Figure 9. *Illustration of the electric field induced by the moving Chapman-Ferraro currents, here modeled by an image dipole (as introduced also in Fig. 1) starting at position $-7.8R_E$ and moving with constant velocity. The direction and relative magnitudes of the electric field are shown with blue arrows. The position of the Earth is shown with a blue sphere.*

that the moving Chapman-Ferraro current system gives rise to compression of the outer radiation belt, which for the given case amounts to approximately 10%.

135 The discussion and derivation of the results of Fig. 10 assume that the motion is solely described by the $\mathbf{E} \times \mathbf{B}/B^2$-motion of the radiation belt particles, with the electric field derived from the motion of the Chapman-Ferraro current system. A sudden impulse-like compression of the radiation belts will excite magnetosonic waves and the heating of the plasma will penetrate deeper into the radiation belts. The asymmetry of the day and night sides will however be well represented by results like those shown in Fig. 10.

140 The Dessler-Parker-Sckopke relations (*Dessler and Parker*, 1959; *Sckopke*, 1966) predict a detectable perturbation of the magnetic field as measured by e.g. ground-based stations, but these theorems refer to symmetric conditions. The asymmetric perturbation illustrated in Fig. 10 will take some time to relax and thermalize at a rotational symmetry (*Summers et al.*, 2012), i.e. of the order of 4-6 h for a localized distribution of 3 MeV electrons to transform into a uniformly distributed ring. Some details concerning the dynamics of the radiation belts are summarized in Appendix C.
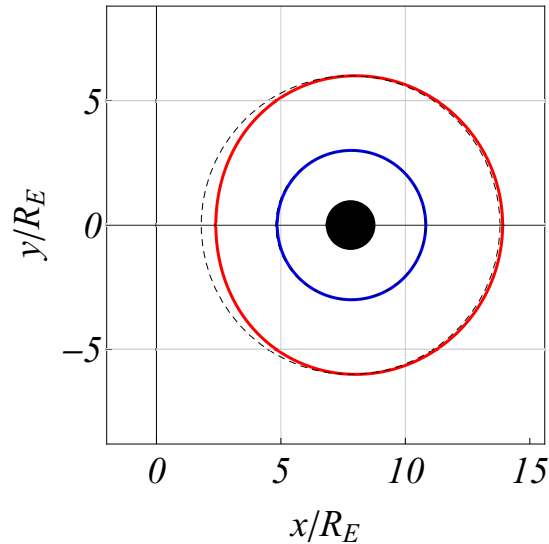
Figure 10. *Illustration of the compression of the radiation belts induced by the moving Chapman-Ferraro currents. The figure illustrates the displacement of the inner and outer boundaries. The plane of the figure is perpendicular to the Earth's magnetic dipole. Thin dashed lines show the initial inner and outer boundaries, here taken at positions 3 and 6 in units of Earth radii, R_E.*

2.2.2 Magnetic field aligned currents

As the radiation belts are compressed, the plasma will be adiabatically heated. The heated plasma component will have an enhanced $\mathbf{B} \times \nabla B$-drift in the azimuthal direction and a corresponding locally enhanced currents, also field aligned currents (*Knight*, 1973; *Lühr and Kervalishvili*, 2021), as illustrated in Fig. 11. The effect of the heating will, however, depend on the initial energy of the particles in the radiation belt. Charged particles in the MeV-range will pass through the compressed region in a time that is negligible compared to the compression time and will not be affected.

Adiabatically heated ions and electrons will leave the compressed region in opposite directions with their increased $\overline{U}_{\nabla B}$-velocities, see also (C1) in Appendix C. Net charges of surplus electrons and ions, respectively, will build up when these particles enter the surrounding colder regions. These excess charges can expand only along magnetic field lines, or be canceled by ions or electrons flowing up from the ionosphere along the same magnetic field lines, see Fig. 11. The adiabatic heating of a finite region (see Fig. 10) will consequently give rise to field aligned currents. The generator is modeled best by an ideal current generator, in contrast to the ideal voltage or potential generator usually assumed for studies of field aligned currents (*Knight*, 1973). The ideal current generator has infinite inner impedance while the voltage generator (ideal battery) has vanishing impedance. It is known (*Garcia et al.*, 2015) that the distinction has important consequences. Numerical simulations of, for instance, ionospheric double layers (*Smith*, 1982) demonstrated the importance of the generator impedance.

To estimate a magnitude of the total field aligned current we can first take $J^{(w)} = \pm e \overline{n}^{(w)} \overline{U}_{\nabla B}^{(w)}$ to be the current density inflow into a small volume element adjacent to the heated region, the charge sign depending on the location of the volume

element. The superscript $^{(w)}$ denotes the heated (warm) region. The current density outflow from the same element is at the same time $J^{(c)} = \pm e\overline{n}^{(c)}\overline{U}^{(c)}_{\nabla B}$ with $^{(c)}$ referring to the cold unheated plasma. Introduce $\mathcal{A}$ as the transverse area of a cross section of the heated volume (see Fig. 10), i.e., a cut in the radial direction along the magnetic field lines. We have the magnitude

165 of the net current into a volume due to the $\nabla B \times \mathbf{B}/B^2$-drift to be $|I| = \mathcal{A}|J^{(w)} - J^{(c)}|$. In order to avoid unlimited charge build-up this current has to be compensated by field aligned currents of the same net magnitude flowing into the ionosphere. Details of the spatial distribution of current densities depend on the geometry and other conditions.
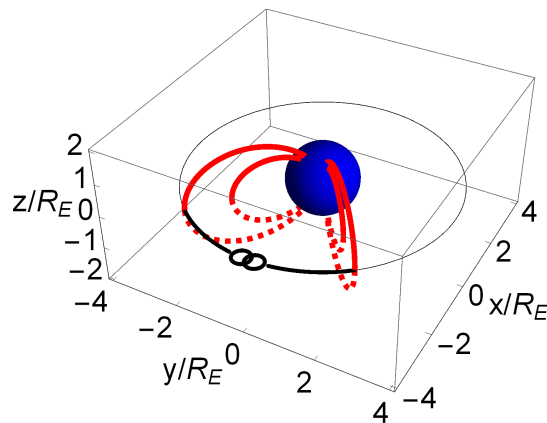
Figure 11. *Diagram for explaining magnetic field aligned currents generated by the asymmetric compression of the radiation belts. Red lines show selected magnetic field lines. The symbol* $-\!\bigcirc\!\bigcirc\!-$ *indicates a current generator.*

The space-time varying electric and magnetic fields generated by the dynamic variations in the position and intensity of the Chapman-Ferraro current system induces currents in the Earth's near ionosphere. A simple model for idealized conditions is

170 outlined in Appendix D.

3 Comparison with observations

The model predictions concerning R and T_0, as well as the damping of the oscillations received numerical confirmation (*Børve et al.*, 2011). The agreement was even better than stated by the authors due an error in the velocity used for normalization in the simulations of their Figs. 9, 10 and 13. In reality the agreement was close to perfect. The numerical model used for

175 the analysis is however in two spatial dimensions and the steady state conditions depended on numerical resistivity and viscosity that dominate model viscosity and resistivity (*Børve et al.*, 2014). The importance of viscosity is different for numerical simulations in 2 and 3 spatial dimensions. Although this does not affect the dynamic features, a more general test would be worthwhile. Later fully 3 dimensional numerical Magneto Hydrodynamic (MHD) simulations (*Desai et al.*, 2021) have given more detailed results supporting the restricted solutions found by *Børve et al.* (2014). There is also a slight difference between

180 the 2 and the 3 dimensional versions of the analytical expressions used in the present work.

The predictions of the model discussed in the foregoing can be compared also to space observations as done in the following. Here we distinguish steady state and dynamic observations.

3.1 Steady state conditions

Inserting typical numbers as $U \approx 3 \times 10^5$ m/s, $n \approx 5 \times 10^6$ m^{-3}, and an average mass equaling the hydrogen mass, $M = $
185 1.66×10^{-27} kg, we find $R \approx 7.2 \times 10^7$ m, or $R \approx 11.2 \, R_E$ in terms of the Earth radius $R_E = 6.4 \times 10^6$ m. The estimate for R are comfortably within the generally accepted range of $R \sim 10 - 15 \, R_E$ (*Kivelson and Russell*, 1995). The model equation (1) implies a closed scaling law for the distance to the magneto-sheet boundary in terms of the solar wind velocity U and the solar wind mass density $n\overline{M}$. Note that there are no free parameters to fit in equation (1), i.e. all are measurable quantities.

3.2 Time varying conditions

190 Fluctuations on the minute time scales are often observed in the magnetosphere in response to strong perturbations in the solar wind. Consistent with a model using nonlinear oscillators (*Børve et al.*, 2011), harmonics of the magnetospheric oscillations are often observed (*Kepko and Spence*, 2003). These are consistent with the strong nonlinear harmonic generation features of the basic model (4). Details of other predictions of the model will here be compared with two sets of space observations.

3.2.1 Event of December 21, 2014.

195 In Fig. 12 we show plasma and magnetic field data from the *Wind* spacecraft illustrating the propagation of a shock in the solar wind, seen at $\sim$18:40 UT. *Wind* is located at $\{197.5, -53.5, -8.8\}$ R_E upstream of Earth. From top to bottom, the plot shows the proton density, bulk speed, and temperature, the dynamic pressure, the components of the magnetic field in geocentric solar magnetospheric (GSM) coordinates, and the storm-time $SymH$ index. Parameters relevant to the shock are given in Table 1. The shock is being driven by an ICME (*Richardson and Cane*, 2010). The magnetic field upstream of the shock (average over
200 3 min) is $\{-0.13, 8.24, -4.02\}$ nT, and the shock normal, using the magnetic coplanarity theorem (*Colburn and Sonett*, 1966) is $\{-0.58, -0.79, -0.21\}$, both in GSE coordinates. This gives an angle between the upstream field and the shock normal, $\Theta_{BN} = 52.7°$, so the shock is quasi-perpendicular. The shock speed is 344.56 km/s, based on Rankine-Hugoniot relations (see *Abraham-Shrauner and Yun* (1976) and references therein). The Mach number of the shock is $\sim$4.

205 The shock gives rise to perturbations of the magnetic field as measured also by ground-based magnetometers. In Fig. 13 we show data the CARISMA magnetometer network in Canada for a 30 min period. Signals from a few other stations are shown in Fig. 14. An abrupt rise in the magnetic field intensity, followed by some irregular oscillations can be seen at about 19:20 UT, where a period of the order of 5–10 min can be noted. The magnitude of the magnetic field perturbations, 10–20 nT are in reasonable agreement with estimates based on Fig. 8. Data from the IMAGE network were also collected, showing somewhat
210 similar results with clear 5 min period oscillations. At the location of the IMAGE stations, the magnetic local time (MLT) at shock arrival is $\sim$22 MLT, i.e., pre-midnight. At substorm onset the stations are prone to the activation of the westward

Magnetic field units	nT	nT	nT
Upstream field	-0.13	8.24	-4.02
Downstream field	-4.28	13.01	-10.39
Velocity units	km/s	km/s	km/s
Upstream velocity	-377.66	-8.18	18.00
Downstream velocity	-447.06	-35.41	22.43
Shock normal	-0.58	-0.79	-0.21

Table 1. *The shock parameters of event December 21, 2014. The vectors are expressed in geocentric solar ecliptic (GSE) coordinates.*

electrojet. In this case substorm activity was excited by the shock arrival under the prevailing negative interplanetary magnetic field (IMF) B_z conditions (this is seen in the IMAGE magnetograms from the pre-midnight sector; these are not shown here).

215 The previous figures 13 and 14 were local. To give a more global overview we show the variation of the signal detected by ground-based stations is illustrated in Fig. 15, showing the component normal with respect to ground with a color code. The radius in the small circles give the relative variation of the tangential component of the magnetic field perturbation. An intense magnetic field perturbation with a large vertical component and simultaneously a small horizontal component will thus be shown with a circle having a small radius. The color is red if the vertical component is into the ground, and blue if it is in the opposite direction. The mapping of the globe is chosen to make the circles having approximately the correct relative

220 magnitudes. When plotting these results we took the first peak maximum after onset of the signal. Note that in general the magnitudes of the horizontal components is larger than the vertical components. We find an overall tendency for positive B_z-values in the northern hemisphere and small or negative B_z-values in the southern hemisphere. The variation across Northern America appears uniform, in particular. The results are in fair agreement with the model, although not perfect. The strongest deviations are found near the magnetic poles.

225 **3.2.2 Event of March 17, 2015.**

In Fig. 16 we show data for 1 day (March 17, 2015) from the *Wind* spacecraft, illustrating the propagation of a shock in the solar wind at ∼5 UT. See also Table 2. The field and plasma data are analyzed in the same manner as for previous shock. The magnetic field upstream of the shock is $\{1.75, 4.59, 8.70\}$ nT and the shock normal, using the magnetic coplanarity theorem (*Colburn and Sonett*, 1966) is $\{0.96, -0.03, -0.28\}$, with both vectors expressed in GSE coordinates. This gives an angle

230 between the upstream field and the shock normal $115.4°$, so the shock is quasi-perpendicular ($\Theta_{BN} = 180° - 115.4° = 64.6°$). The shock speed is 601.3 km/s, based on Rankine-Hugoniot relations, see *Abraham-Shrauner and Yun* (1976) and references therein. The speed of plasma along shock normal is 405.211 km/s.

At the time of the sudden impulse seen in the $SymH$ index (at 4:46 UT, March 5) due to the shock seen in Fig. 16, ground

235 stations observed magnetic field variations. Results from the set of the IMAGE magnetometers are shown in Fig. 17. The
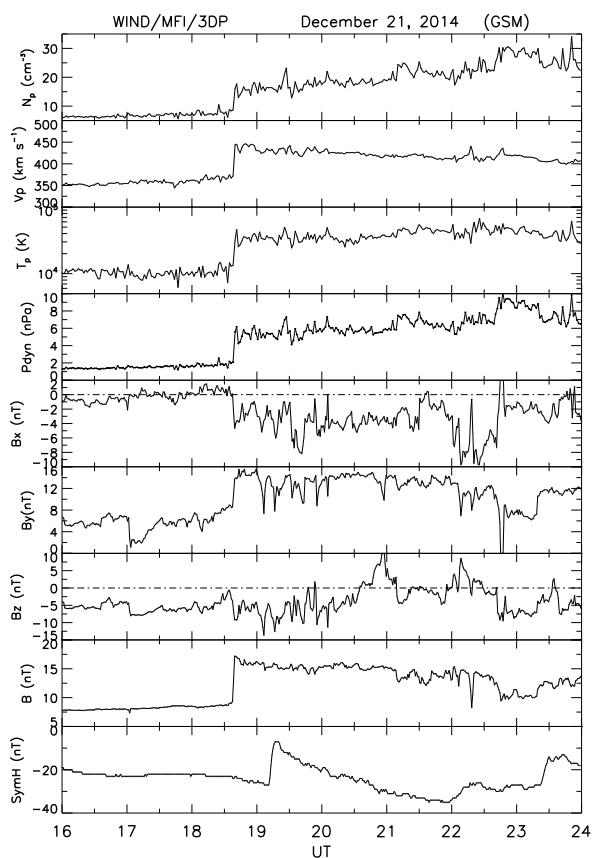
Figure 12. *Data from the Wind satellite showing shock propagation in the solar wind to be compared with the results in Fig. 16.*

Magnetic field units	nT	nT	nT
Upstream field	1.75	4.59	8.70
Downstream field	1.98	11.63	20.52
Velocity units	km/s	km/s	km/s
Upstream velocity	-421.23	27.46	2.71
Downstream velocity	-533.99	5.44	33.34
Shock normal	0.96	-0.03	-0.29

Table 2. *The shock parameters of event March 17, 2015. The vectors are expressed in geocentric solar ecliptic (GSE) coordinates.*
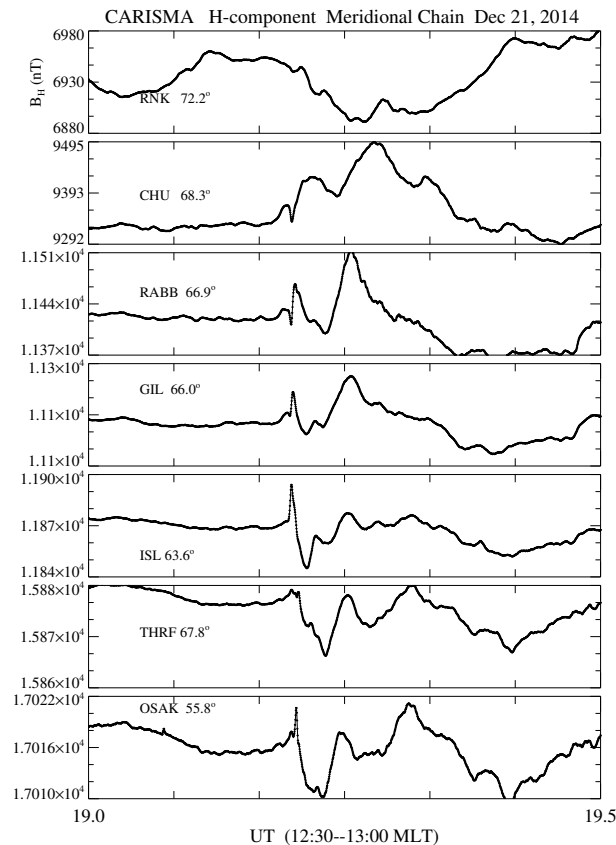
Figure 13. *Data from the CARISMA magnetometer network in Canada with the stations specified by their acronyms, RNK, CHU, etc. Apart from the top curve, which refers to an open magnetic field line, we see the pulse arrival followed by low frequency, ∼5 min period oscillations best seen at CGM Latitudes 67.8° and 55.8^{c}irc. The mean values are not subtracted.*

magnetic local time (MLT) range of the stations in the UT range plotted is 7-9 MLT, i.e., they are sampling dawnside local times. Figure 17 shows magnetograms from a wide range of latitudes extending from the polar cap to middle latitudes. The negative/positive deflections at the northernmost stations on Svalbard (NAL to BJN) are related to the activation of lobe cell convection under the strongly northward interplanetary magnetic field (IMF) condition at the time of the shock arrival (see Fig. 16). Our focus is on the impulse/oscillation at lower latitudes during the interval 04:46-04:50 UT, which is more directly related to the IP shock.

After a short transition we see small-amplitude, damped oscillations of periods 4-6 min at 4:46 UT.

The signal obtained by ground stations at various local times is illustrated in Fig. 18. Here the MLTs are: at GUA, 14:30 MLT, at DLT, about 12 MLT and at M08 about 22 MLT. Note the vertical scales are larger than those of Fig. 14.

The signal obtained by ground stations at various local times is illustrated in Fig. 19. As in Fig. 15, we show the component normal with respect to ground with a color code. Positive values point into the Earth also here. The results near the magnetic
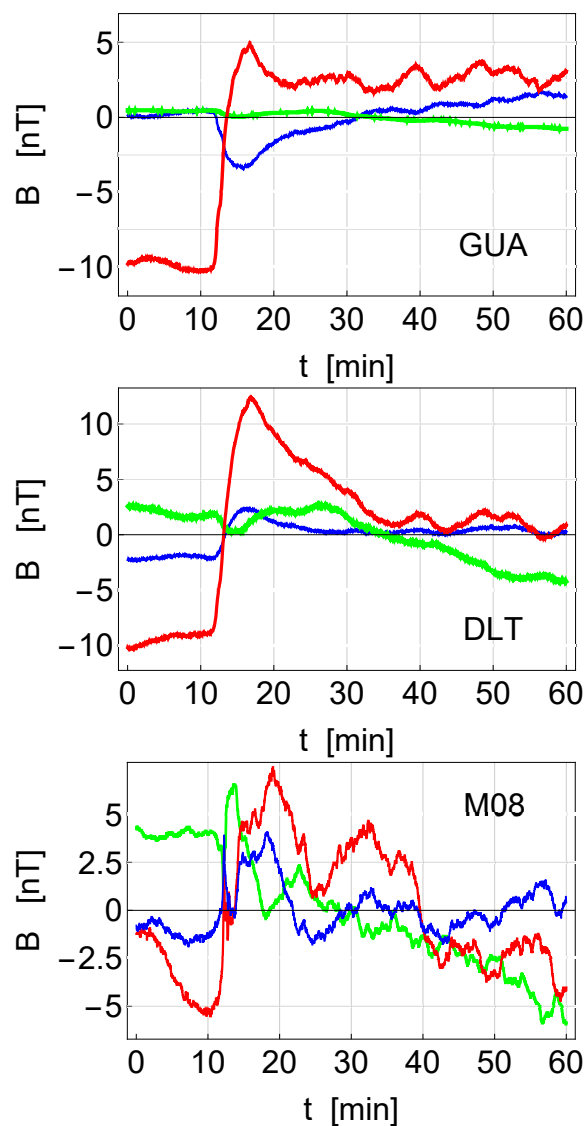
Figure 14. *Variations of the magnetic field components B_x (red), B_y (green) and B_z (blue) as observed by the GUA (Guam) and DLT (Dalat, Vietnam) ground stations in response to the shock seen in Fig. 12. Similar data from the M08 (San Antonio) station are shown as well. The averages are subtracted on all figures. The data were obtained by SuperMAG (Gjerloev, 2012). The first data-point is at 2014-12-21, 19:00 UTC. We note some heavily damped oscillations in all figures, with oscillations with 5 - 10 min periods discerned.*
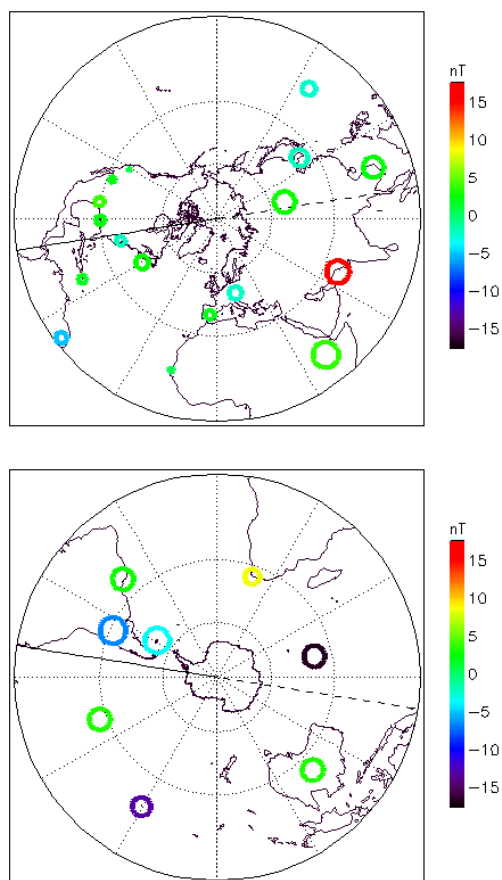
Figure 15. *Variations of the magnetic field components as detected on ground on 2014-12-21. The data refer to the first peak value after the shock arrival in figures like Fig. 14. North and South America are facing the Sun at this time. The data were obtained by SuperMAG (Gjerloev, 2012).*
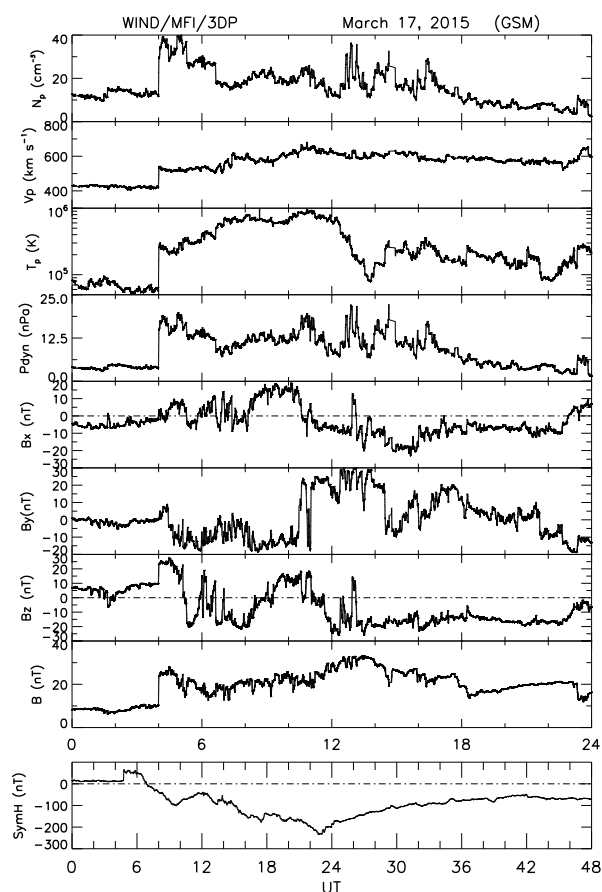
Figure 16. The figure shows *Wind* and ground-based data for the period March 17-18, 2015. The format is the same as Fig. 12, except that the proton beta in the last panel of Fig. 12 has been replaced by the storm time $SymH$ index. At ∼4:03 UT, a sharp rise is seen in Np, p, Tp, $Pdyn$ and B, indicative of a shock passing the *Wind* spacecraft. The ground response is recorded ~ 43 min later with a rise in the index $SymH$. The configuration resulted in a geomagnetic storm reaching peak values of -234 nT. For completeness and later reference we show $SymH$ results separately for a duration of 48 h.

poles have magnitudes typically up to 2–3 times larger than the average of the values shown, and also the time variations found there can be more irregular. The same comments apply also to Fig. 15 and the values for these regions are not shown. These features are believed to be due to field aligned currents (*Knight*, 1973; *Lühr and Kervalishvili*, 2021), where the present model
250 only gives some qualitative results, see Fig. 11. The spatial variations in the magnetic field perturbations seen in Fig. 19 are larger and non-uniform compared to those found in Fig. 15.
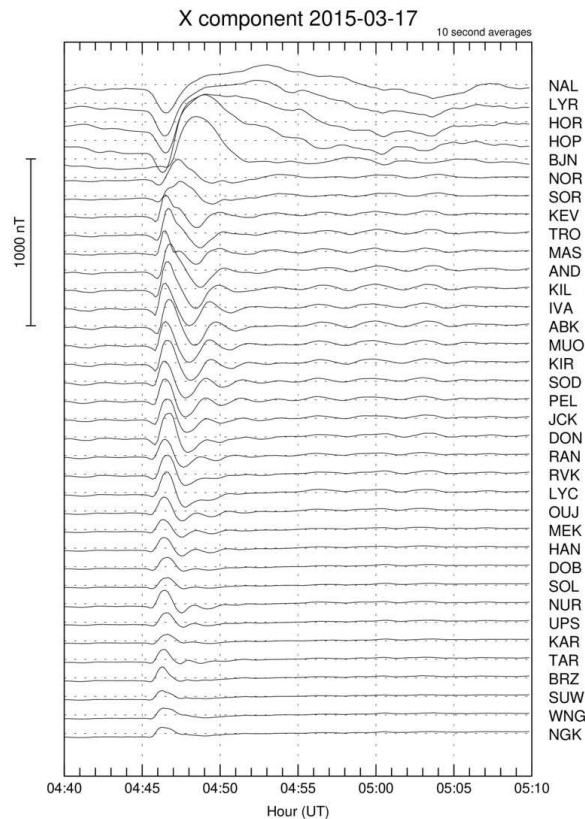
Figure 17. *X-component of the signals detected at the IMAGE stations at the event of March 17, 2015. Each curve is labeled by the acronym for the appropriate station. The data are obtained near 04:46 UT, i.e. around 07:46 MLT (magnetic local time), near dawn. The questions relating to the substorm current wedge mentioned earlier do not apply for this case.*

For the dynamics in the radiation belts we have data from the Van Allen Probes (formerly known as the Radiation Belt Storm Probes (RBSP)), with the relevant positions of the two satellites shown in Fig. 20. The satellites measure the electric fields as shown in Fig. 21 to be compared with the model results in Fig. 9. From (1) we have for this case $R \approx 6 \times 10^7$ m, and from
255 (3) we find $T_0 \approx 250$ s, or approximately 4 min. The magnetopause moves approximately $0.05R$ within a time $T_0/5$, giving a velocity $0.25R/T_0 \approx 6 \times 10^4$ m s^{-1} or 60 km s^{-1} using the estimate from Fig. 7. To represent the temporally changing magnetic field, the image dipole has to move with a velocity U twice this value. The magnetic field from the moving image

dipole has to be taken at a distance of approximately $1.5R$ from it, i.e. at a position somewhere between the Earth and the magnetopause, giving $B \approx 20$ nT. With $E \approx UB$ we estimate $E \approx 2$ mV m^{-1} in the $\widehat{\mathbf{y}}$-direction. In magnitude and direction,

260 this value is reasonably close to the observed value of $E \approx 4$ mV m^{-1} in the $\widehat{\mathbf{y}}$-direction, see Fig. 21. The E_y component is the dominant one and in the positive y-direction, consistent with results in Fig. 9. We note also some heavily damped electric field oscillations with approximately 5 min period. A small observed z-component of the electric field can be explained by a small tilt of the magnetic dipole axis, which was not included in the model analysis. The electric field results are close to the predicted values both in magnitude and direction. The two satellites are at similar distances from the magnetopause and detect

265 similar electric fields. They are however placed at different positions with respect to the radiation belts so the observed particle energy variations are different.

The time variation of the energy distribution of the plasma in the Earth's radiation belt was measured as shown in Figs. 21, 22 and 23. It is interesting to note that it is the Van Allen Probe A that detects the strongest electron heating in Fig. 21. The REPT and magEIS instruments on probe B show particle heating at a somewhat smaller level compared to probe A. The

270 heating signal arrives a little earlier (by approximately 1 min) at probe B, see Fig. 20 for the probe positioning. The electrons heated by the compression of the radiation belts as shown in Fig. 10 will have their $\mathbf{B} \times \nabla B$-drift in the positive y-direction in Fig. 20. These electrons have to propagate $\sim (4/3)\pi R_E$ to reach satellite A. The estimate in Appendix C is in reasonable agreement with the time delay found in Fig. 21.

4 Conclusion

275 A simple model for illustrating the near-Earth magnetospheric static as well as dynamic features has been presented. The model predicts the distance between the Earth and the magnetopause (stand-off distance) without introducing free parameters, as well as some dynamic features, in particular the frequency of magnetospheric oscillation in response to an impulse in the solar wind. A damping of the oscillations is predicted. This damping is not caused by dissipation but is an inherent feature of phase relations in the model. For testing the predictions of the model we considered two events, i.e., two geomagnetic storms: one moderate

280 for the December 21, 2014 with $SymH \sim -70$ nT and a strong one occurring at March 17, 2015 with $SymH \sim -237$ nT. The magnetospheric response on the impact of them was similar, but with significant differences in the details. The agreement with our model was best for the moderate shock. The magnetic field perturbations in Fig. 18 are significantly larger than those shown in Fig. 14 as expected.

In the last panel of Fig. 16 we plot the temporal profile of the $SymH$ index over a 2-day period. $SymH$ is a measure of the

285 strength of the ring current. In this case it has a two-dip structure, indicating that we have a 2-dip storm (*Kamide et al.*, 1998). The weaker dip occurs at $\sim$9:15 UT, March 17. This caused a major storm already. The $SymH$ then recovers for $\sim$14 hrs, only to decrease again and reach a new and deeper minimum at $\sim$21 UT, March 17. The first dip is caused by the shock compressing $B_z < 0$ (GSM) fields. The second one is caused by the long ($\sim$10 hrs) $B_z < 0$ phase inside the ICME itself. Both strengths correspond to major geomagnetic storms, but the second one almost reaches "superstorm" values ($SymH < -250$ nT). The
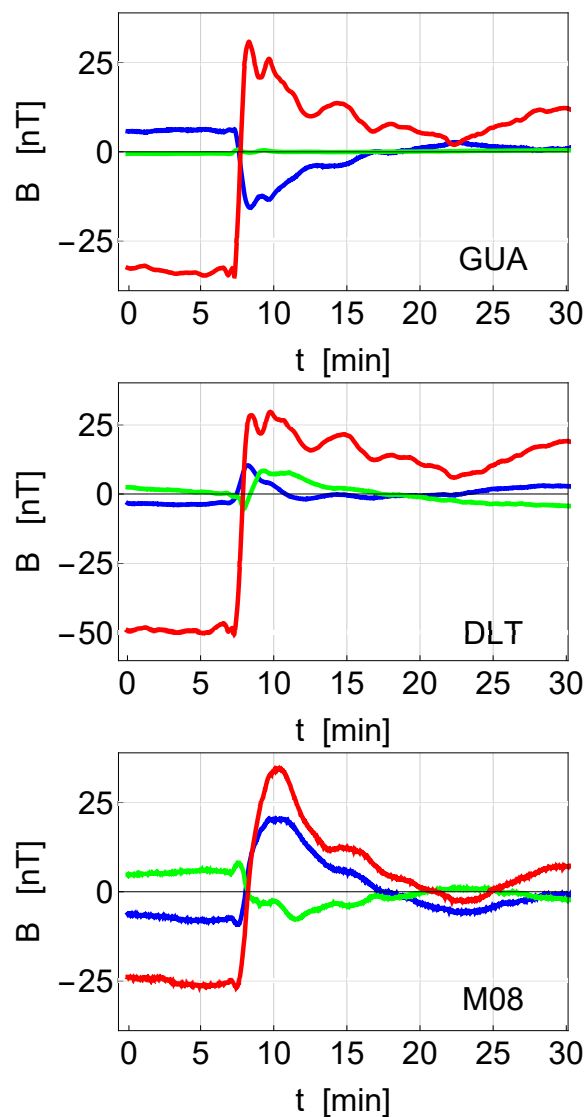
Figure 18. *Variations of the geomagnetic field components, B_x (red), B_y (green) and B_z (blue), as observed by ground stations GUA (GUAM), DLT (Dalat) and MO8 (San Antonio) in response to the shock seen by Wind (Fig. 16). The magnetic local times being sampled are 4 MLT (GUA), 3 MLT (DLT) and 12 MLT (MO8). The averages are subtracted in all figures. The first data-point is at 2015-03-17, 04.38 UTC. Notice the damped ~ 5 min period oscillations in the figures. See also Fig. 14 for comparison.*
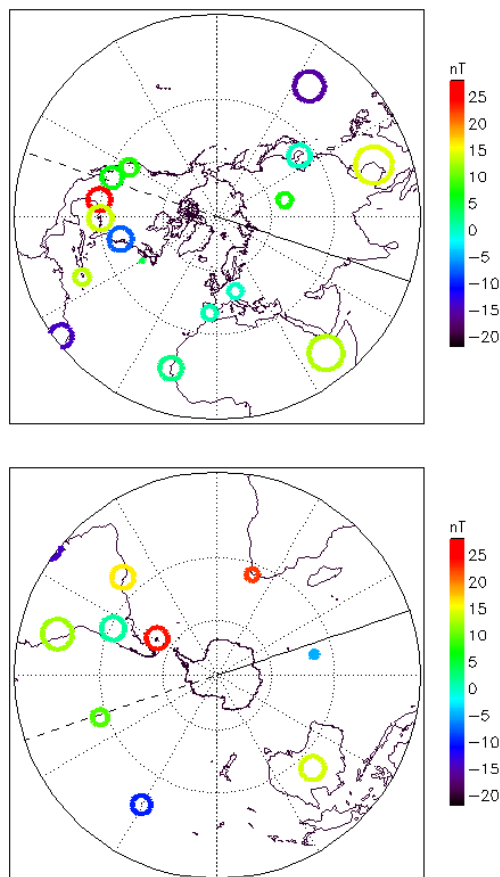
Figure 19. *Variations of the magnetic field components as detected on ground on 2015-03-17. The data refer to the first peak value after the shock arrival in figures like Fig. 18. The data were obtained by SuperMAG (Gjerloev, 2012).*

same thing holds for Dec 21, 2014 event, only the $SymH$ dips are here much weaker ($\sim$35 and $\sim$60 nT) and they are separated by $\sim$8 hrs (not shown).

The main conclusion of the present study can be summarized in few words: "Three dipoles suffice for the lowest order modeling of the near-Earth magnetosphere", one, $\mathbf{Q}_E$, for the Earth's magnetic field and two image dipoles, where one, $\mathbf{Q}_I$, is placed in the solar wind, the other, $\mathbf{Q}_S$, in the Earth's interior see Appendix D. We have $\mathbf{Q}_I$ and $\mathbf{Q}_E$ to be parallel so their magnetic field contributions add at the Earth's surface. The interior dipole $\mathbf{Q}_S$ is anti-parallel to $\mathbf{Q}_E$ so that the radial component of the magnetic field cancels in the the ionosphere at a radius here taken to be R_E to sufficient accuracy.

One partial result of the present analysis is an emphasis of the strongly nonlinear features and damping of the magnetospheric oscillations. These are explained here by the basic properties of a simple physical model. The observed frequencies and damping rates seen in, e.g., the CARISMA data in Fig. 13 and in part also the IMAGE data in Fig. 17 are in good agreement
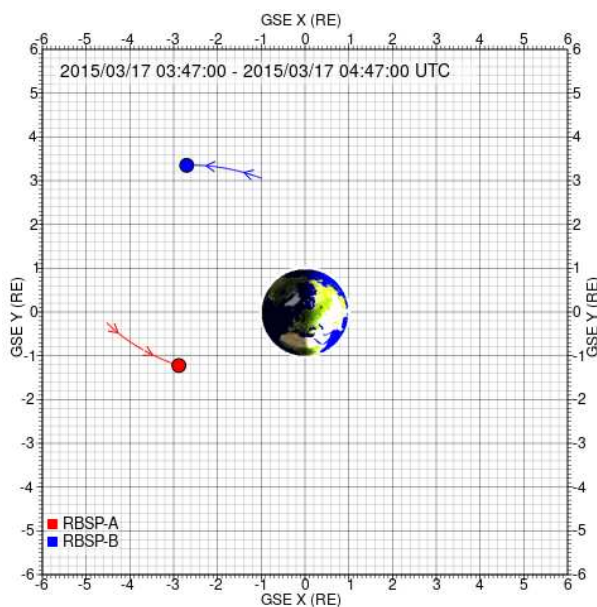
Figure 20. *Positioning of the two Van Allen satellites with A at approximately the position $(-2.8, -1.2)$ and B at $(-2.7, 3.3)$. The orbits are close to being confined to the $x - y$-plane, so only the projection of the orbits on this plane is shown. The satellite positions are shown at time 04.46 UTC. The duration of the trajectory shown is 1 h. The Sun is to the right in this presentation.*

300 with the model results. Ground-based results by SuperMAG are in similarly fair agreement, see Fig. 14 and also Fig. 18. By inspection of Figs. 12 and 16 we find that there are no systematic long period oscillations of $|\mathbf{B}|$ following the shock structure. The oscillations observed in figures like 13 or 18 are thus natural for the system and not due to some external forcing. The model also predicts the magnitudes of magnetic and electric fields detected by ground stations and satellites to better than an order of magnitude. We consider this to be satisfactory. The ideas put forward in the present study can be applied to any

305 magnetized planet like the Earth, orbiting a star like the Sun.

The main limitations of the model are found in:

– its inability to account for the far magnetotail conditions, the dynamics in particular. A cross-tail current is not included in the model.

– magnetic field line reconnection (*Califano et al.*, 2009) is missing in the model. This is important when the interplanetary

310 magnetic field has a downward component.

– field aligned currents can at best be argued qualitatively.

– surface eigenmodes of the dayside magnetopause (*Archer et al.*, 2019; *Hwang*, 2015; *Hartinger et al.*, 2015) are not accounted for. These will give rise to additional, presumably small amplitude, oscillations to the modes described in our work.
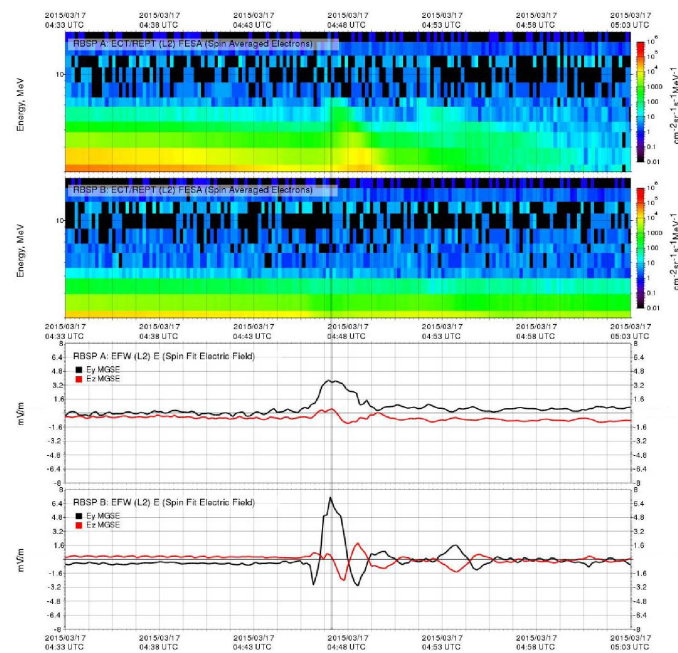
Figure 21. *Temporal variation of the electron energy distribution (top) and electric field components (bottom) as detected by the two Van Allen Probes. A thin vertical gray reference line indicates the arrival time of the electromagnetic pulse at the Van Allen satellites. Note the time-lag of the detected electron heating. The lowest energy particles are delayed most. For 2 MeV particles the delay is approximately 50 s as found on satellite A. There is only negligible electron energization detected by satellite B. Strongly damped oscillation in the electric fields have a period of approximately 2 min.*

315   – field aligned currents are argued only qualitatively, see Fig. 11. These will be important near the magnetic poles, in particular.

We believe the present model deserves close scrutiny. The predictions can be compared to other related data which can be classified according to the details such as $SymH$ for the observed shocks.

Acknowledgment. Valuable communications with Jesper Gjørlev concerning use and interpretation of SuperMAG data are
320   gratefully acknowledged. Magnar Gullikstad Johnsen offered valuable comments. CJF was supported by NASA Wind grant 80NSSC19K1293 and 80NSSC20K0197. Figure 14 presented in this paper rely on the data collected at GUA, DLT, and M08. We thank Institut de Physique du Globe de Paris and United States Geological Survey for supporting its operation and INTERMAGNET for promoting high standards of magnetic observatory practice (www.intermagnet.org). Data from the Van Allen probes were accessed at the Science Gateway, maintained by the Johns Hopkins University Applied Physics Laboratory.
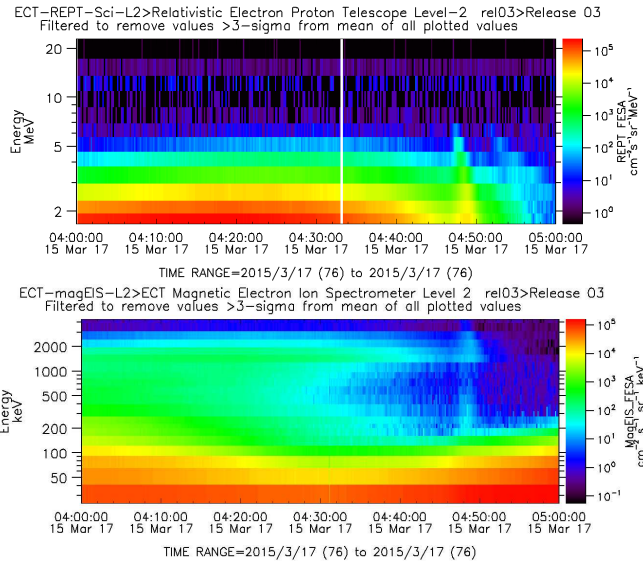
Figure 22. *Temporal variation of the energy distribution of the plasma particles forming the radiation belts as detected by the Van Allen Probe A. Two energy resolutions of the same event are shown, illustrating that it is the lowest energy particles that are heated most. Data from the REPT and magEIS instruments are shown.*
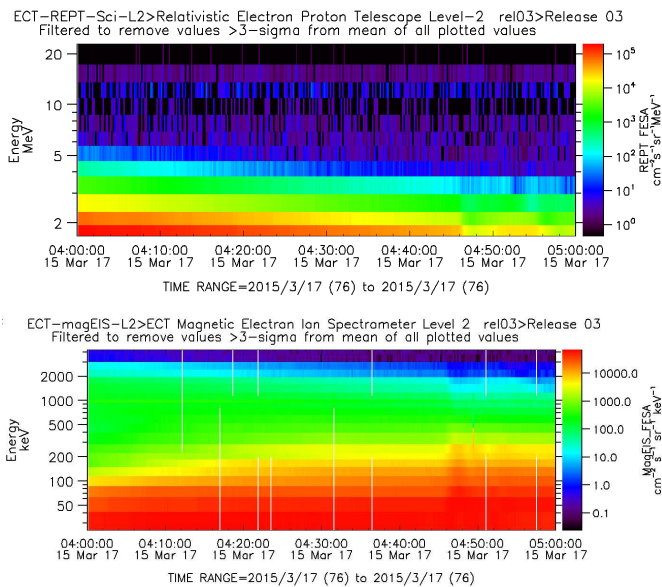
Figure 23. *Temporal variation of the energy distribution of the plasma particles forming the radiation belts as detected by the Van Allen Probe B. See also Fig. 22. Some thin white vertical lines are data-gaps.*

325   *Author contributions.*   All authors contributed to the data collection, analysis and manuscript preparations. HS, PES, and CJF mostly to the data collection, HLP and JKT mostly to preparation of manuscript and figures.

Competing interests.   The authors declare that they have no conflict of interest.

References

Abraham-Shrauner, B., and S. H. Yun, Interplanetary shocks seen by Ames Plasma Probe on Pioneer 6 and 7, *J. Geophys. Res. (1896-1977)*, *81*, 2097–2102, 1976, doi:10.1029/JA081i013p02097.

Alfvén, H., *Cosmical Electrodynamics*, Oxford University Press, London, 1950.

Araki, T., A physical model of the geomagnetic sudden commencement, in *Solar Wind Sources of Magnetospheric Ultra-Low-Frequency Waves*, vol. 81 of *Geophysical Monograph*, pp. 183–200, The American Geophysical Union, Washington, DC, 1994.

Archer, M. O., T. S. Horbury, J. P. Eastwood, J. M. Weygand, and T. K. Yeoman, Magnetospheric response to magnetosheath pressure pulses: A low-pass filter effect, *J. Geophys. Res.: Space Physics*, *118*, 5454–5466, 2013, doi:10.1002/jgra.50519.

Archer, M. O., , M. D. Hartinger, F. Plaschke, and V. Angelopoulos, Direct observations of a surface eigenmode of the dayside magnetopause, *Nature Communications*, *10*, 615, 2019, doi:10.1038/s41467-018-08134-5.

Børve, S., H. Sato, H. L. Pécseli, and J. K. Trulsen, Minute-scale period oscillations of the magnetosphere, *Ann. Geophys.*, *29*, 663–671, 2011, doi:10.5194/angeo-29-663-2011.

Børve, S., H. Sato, H. L. Pécseli, and J. K. Trulsen, Low frequency oscillations of the magnetosphere, in *2014 XXXIth URSI General Assembly and Scientific Symposium (URSI GASS)*, pp. 1–3, 2014, doi:10.1109/URSIGASS.2014.6929936.

Buckingham, E., On physically similar systems; illustrations of the use of dimensional equations, *Phys. Rev.*, *4*, 345–376, 1914, doi:10.1103/PhysRev.4.345.

Califano, F., M. Faganello, F. Pegoraro, and F. Valentini, Solar wind interaction with the Earth's magnetosphere: the role of reconnection in the presence of a large scale sheared flow, *Nonlinear Processes Geophys.*, *16*, 1–10, 2009, doi:10.5194/npg-16-1-2009.

Chen, F. F., *Introduction to Plasma Physics and Controlled Fusion*, 3 ed., Springer, Heidelberg, 2016.

Chen, L., and A. Hasegawa, A theory of long-period magnetic pulsations: 2. impulse excitation of surface eigenmode, *J. Geophys. Res.*, *79*, 1033–1037, 1974, doi:10.1029/JA079i007p01033.

Colburn, D. S., and C. P. Sonett, Discontinuities in the solar wind, *Space Sci. Rev.*, *5*, 439,506, 1966, doi:10.1007/BF00240575.

Desai, R. T., et al., Interplanetary shock-induced magnetopause motion: Comparison between theory and global magnetohydrodynamic simulations, *Geophys. Res. Lett.*, *48*, e2021GL092,554, 2021, doi:10.1029/2021GL092554.

Dessler, A. J., and E. N. Parker, Hydromagnetic theory of geomagnetic storms, *J. Geophys. Res.*, *64*, 2239–2252, 1959, doi:10.1029/JZ064i012p02239.

Farrugia, C. J., and F. T. Gratton, Aspects of magnetopause/magnetosphere response to interplanetary discontinuities, and features of magnetopause Kelvin-Helmholtz waves, *J. Atmospheric Solar-Terrestrial Phys.*, *73*, 40–51, 2011, doi:10.1016/j.jastp.2009.10.008.

Freeman, M. P., N. C. Freeman, and C. J. Farrugia, A linear perturbation analysis of magnetopause motion in the Newton-Busemann limit, *Ann. Geophysicae*, *13*, 907–918, 1995.

Garcia, O. E., E. Leer, H. L. Pécseli, and J. K. Trulsen, Magnetic field-aligned plasma currents in gravitational fields, *Ann. Geophysicae*, *33*, 257–266, 2015, doi:10.5194/angeo-33-257-2015.

Gjerloev, J. W., The SuperMAG data processing technique, *J. Geophys. Res.: Space Phys.*, *117*, A09,213, 2012, doi:10.1029/2012JA017683.

Hartinger, M. D., F. Plaschke, M. O. Archer, D. T. Welling, M. B. Moldwin, and A. Ridley, The global structure and time evolution of dayside magnetopause surface eigenmodes, *Geophysical Res. Letters*, *42*, 2594–2602, 2015, doi:10.1002/2015GL063623.

Hwang, K.-J., Electron magnetopause waves controlling the dynamics of Earth's magnetosphere: Dynamics and turbulence, *J. Astronomy Space Sci.*, *32*, 1–11, 2015, doi:10.5140/JASS.2015.32.1.1.

365   Kamide, Y., N. Yokoyama, W. Gonzalez, B. T. Tsurutani, I. A. Daglis, A. Brekke, and S. Masuda, Two-step development of geomagnetic storms, *J. Geophys. Res. Space Physics*, *103*, 6917–6921, 1998, doi:10.1029/97JA03337.

Kepko, L., and H. E. Spence, Observations of discrete, global magnetospheric oscillations directly driven by solar wind density variations, *J. Geophys. Res.*, *108*, 1257, 2003, doi:10.1029/2002JA009676.

Kivelson, M. G., and C. T. Russell (Eds.), *Introduction to Space Physics*, Cambridge University Press, UK, 1995.

370   Kivelson, M. G., J. Etcheto, and J. G. Trotignon, Global compressional oscillations of the terrestrial magnetosphere - the evidence and a model, *J. Geophys. Res.*, *89*, 9851–9856, 1984, doi:10.1029/JA089iA11p09851.

Knight, S., Parallel electric fields, *Planetary Space Science*, *21*, 741–750, 1973, doi:10.1016/0032-0633(73)90093-7.

Korotova, G. I., and D. G. Sibeck, A case study of transit event motion in the magnetosphere and in the ionosphere, *J. Geophys. Res.*, *100*, 35–46, 1995, doi:10.1029/94JA02296.

375   Lühr, H., and G. Kervalishvili, *Field-Aligned Currents in the Magnetosphere-Ionosphere*, chap. 13, pp. 193–205, American Geophysical Union (AGU), 2021, doi:10.1002/9781119815624.ch13.

Pécseli, H. L., *Waves and Oscillations in Plasmas*, Taylor & Francis, London, 2012.

Plaschke, F., K.-H. Glassmeier, D. G. Sibeck, H. U. Auster, O. D. Constantinescu, V. Angelopoulos, and W. Magnes, Magnetopause surface oscillation frequencies at different solar wind conditions, *Ann. Geophysicae*, *27*, 4521–4532, 2009, doi:10.5194/angeo-27-4521-2009.

380   Richardson, I. G., and H. V. Cane, Near-Earth interplanetary coronal mass ejections during Solar cycle 23 (1996 - 2009): Catalog and summary of properties, *Solar Phys.*, *264*, 189–237, 2010, doi:10.1007/s11207-010-9568-6.

Sckopke, N., A general relation between the energy of trapped particles and the disturbance field near the Earth, *J. Geophys. Res.*, *71*, 3125–3130, 1966.

Sibeck, D. G., et al., The magnetospheric response to 8-minute period strong-amplitude upstream pressure variations, *J. Geophys. Res.*, *94*,
385   2505–2519, 1989, doi:10.1029/JA094iA03p02505.

Smith, R. A., A review of double layer simulations, *Physica Scripta*, *T2A*, 238–251, 1982, doi:10.1088/0031-8949/1982/t2a/031.

Song, P., C. T. Russell, J. T. Gosling, M. Thomsen, and R. C. Elphic, Observations of the density profile in the magnetosheath near the stagnation streamline, *Geophys. Res. Lett.*, *17*, 2035–2038, 1990, doi:10.1029/GL017i011p02035.

Southwood, D. J., and M. G. Kivelson, The magnetohydrodynamic response of the magnetospheric cavity to changes in solar wind pressure,
390   *J. Geophys. Res.: Space Phys.*, *95*, 2301–2309, 1990, doi:10.1029/JA095iA03p02301.

Spreiter, J. R., A. L. Summers, and A. Y. Alksne, Hydromagnetic flow around the magnetosphere, *Planetary and Space Science*, *14*, 223–250, 1966, doi:10.1016/0032-0633(66)90124-3.

Stratton, J. A., *Electromagnetic Theory*, McGraw-Hill Book Company, 1941.

Summers, D., I. R. Mann, D. N. Baker, and M. G. Schulz (Eds.), *Dynamics of the Earth's Radiation Belts and Inner Magnetosphere*, vol.
395   Geophysical Monograph, 199, John Wiley, Washington, D.C., 2012.

Walker, R. J., and C. T. Russell, *Introduction to Space Physics*, chap. 6: Solar-wind interactions with magnetized planets, pp. 164–182, Cambridge University Press, Cambridge, UK, 1995.

Appendix A: Generalization of the model

In empty space we approximate the Earth's magnetic field by a simple dipole, here written in spherical coordinates

$$400 \quad B_\phi = 0, \quad B_\theta = \mu_0 Q_E \frac{\cos\lambda}{4\pi r^3}, \quad B_r = \mu_0 Q_E \frac{2\sin\lambda}{4\pi r^3}, \tag{A1}$$

in terms of the angle λ measured from the magnetic equator. We introduced the magnetic dipole moment Q. For the Earth we have $Q_E \approx 8 \times 10^{22} \, \mathrm{A\,m^2}$.
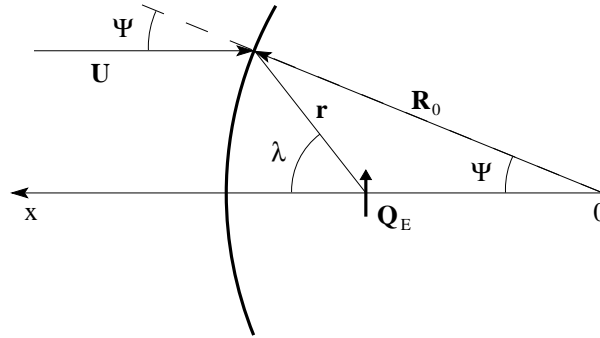
Figure A1. *Illustration of coordinate system for a modified model of the Magnetospheric interface with $\mathbf{Q}_E$ being an equivalent dipole for the Earth's magnetic field.*

Assume that the cut in interface between the solar wind and the Earth's magnetosphere can be approximated locally by a circle with radius R_0, see Fig. A1. The angle between $\mathbf{R}_0$ and the line connecting the Earth and the Sun is Ψ. At an angular position (r, λ) on the interface, see Fig. A1, we can require (at least for small Ψ, away from the cusp-points) a balance in the form

$$\overline{M}nU^2\cos^2\Psi = \frac{1}{2\mu_0}B^2(r,\lambda). \tag{A2}$$

The expression states that the normal component of the solar wind "RAM"-pressure balances the magnetic field pressure, keeping in mind that the magnetic field lines are parallel to the interface. The magnetic field on the Earth-ward side of the interface results from the sum of the B-fields from the Earth's magnetic dipole (A1) and an image dipole. Due to the manageable boundary conditions for potentials and electric fields, the method of images is relatively simple for electric point charges, dipoles, etc., in the vicinity of ideally conducting surfaces. For magnetic dipoles, and higher order multi-poles, the corresponding problems are simple only for some special cases, a plane boundary being one of them.

To obtain an approximation for the magnetic field between the Earth and a curved magnetosphere we take two parallel dipoles, the Earth's magnetic dipole $\mathbf{Q}_E$ and an image dipole $\mathbf{Q}_I$ at positions x_E and x_I, respectively. Introducing the magnetic

field from a dipole (A1) we find that to lowest approximation $\mathbf{Q}_I \approx \mathbf{Q}_E(R_0/x_E)^3$ and the total magnetic field

$$
\mathbf{B}(\mathbf{r}) = \frac{\mu_0 Q_E}{4\pi}\left(\frac{1}{|\mathbf{r} - x_E\widehat{\mathbf{x}}|^3}\right.
$$
$$
\left. + \left(\frac{R_0}{x_E}\right)^3 \frac{1}{|\mathbf{r} - x_E(R_0/x_E)^2\widehat{\mathbf{x}}|^3}\right), \tag{A3}
$$

a result that can be derived from the related problem for an electric dipole near a conducting sphere. The first term gives

420 the Earth magnetic field, the second is the image field. We have $r = \sqrt{R_0^2 + x_E^2 - 2R_0 x_E \cos\Psi}$ and $\cos\lambda = (R_0/r)\sin\Psi$. Introducing (A3) in (A2) it is convenient to define a coefficient $C \equiv 2(4\pi)^2\overline{M}nU^2/(\mu_0 Q_E^2)$.
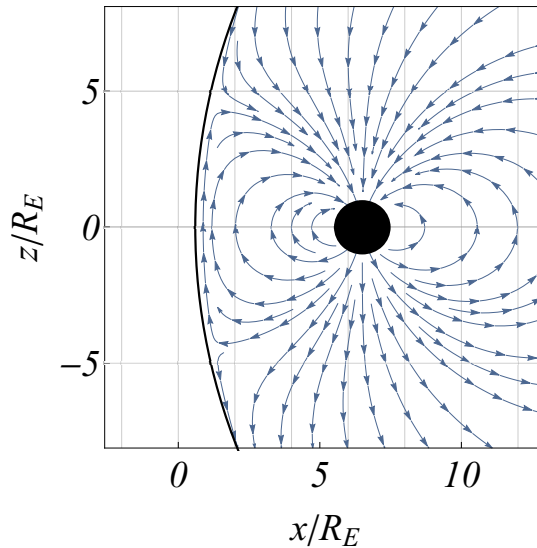
Figure A2. *Illustration of a generalization of the results from Fig. 1 where the image method is extended to account for a self-consistent curvature of the interface between the solar wind and the Earth's magnetic field.*

We optimize the dipole position x_E and the radius of curvature R_0 in such a way that (A2) is fulfilled for given Q_E, n, U and $\overline{M}$, at least to lowest order in expansions of the angle Ψ. The origin of the coordinate system is not specified but here determined through R_0 and x_E. We could choose to place the origin at the Earth, but the analytical expressions will

425 become more complicated, and we would then have to determine R_0 as well as the position for the radius of curvature. For the stagnation point of the solar wind at $(x, z) = (R_0, 0)$ the expression (A2) gives the relation $n\overline{M}U^2 = B^2(R_0, 0)/2\mu_0 = 2\mu_0 Q_E^2(4\pi)^{-2}(x_E - R_0)^{-6}$, in particular. This is consistent with the result of *Børve et al.* (2011), since $R - x_E$ is the distance between the Earth and the interface between the solar wind and the magnetopause. This particular result can be written as $R_0 - x_E = \left(\mu_0 Q_E^2/(8\pi^2 n\overline{M}U^2)\right)^{1/6} = 4\,C^{-1/6}$. From (A2) we find also as an approximate result $R_0 = (19 + 6\sqrt{10})x_E \approx$

430 $38x_E$, implying $R_0 \approx 4.11\,C^{-1/6}$ and $x_E \approx 0.11\,C^{-1/6}$. A stronger solar wind pressure gives a smaller radius of curvature. As the solar wind pressure decreases, i.e. $n\overline{M}U^2 \to 0$, we have $C^{-1/6} \to \infty$ and $R_0 \to \infty$ in such a way that $(R_0 - x_E) \to \infty$. We find these latter results to be intuitively reasonable. The approximation works best when $R_0 - x_E$ is small compared to R_0.

An example of the modified model with a curved interface between the solar wind and the Earth magnetic field is shown in
Fig. A2.

435 An impulse in the solar wind, be it in velocity or density, or both, will give rise to a reduction in the distance $R_0 - x_E$, but
at the same time it will induce also a change in the curvature R_0 of the part of the magnetosphere facing the sun. Within the
present model there is no anisotropy in this curvature: it is the same in the plane parallel and perpendicular to the direction of
the Earths magnetic dipole. The modified model can not account for the formation of the magnetotail.

Appendix B: Dimensional arguments

440 Some results can be derived from simple dimensional arguments (*Buckingham*, 1914). Consider for instance the distance
between the Earth and the magnetopause. The basic parameters are here the solar wind ram pressure $n\overline{M}U^2$ where we note
that the solar wind density and velocity will always appear in this combination so there is no generality gained by taking the
variables separately. Similarly, μ_0 and Q will also appear together, but since μ_0 also enters the magnetic pressure it has to be
included explicitly as well. The mass loading will be here ρD. The dimension matrix for the problem is given by the table

	$n\overline{M}U^2$	R	$\mu_0 Q$	μ_0	ρD	T_0
T	-2	0	-2	-2	0	1
L	-1	1	3	1	-2	0
M	1	0	1	1	1	0
A	0	0	-1	-2	0	0

For a time stationary problem where the magnetopause is at rest we have time T_0 in the sixth column to vanish from the
problem, and similarly the inertia term ρD can not have any effect either. Then the first and third rows are proportional. We
write from left to right in terms of the variables on the top in the dimension matrix

$$\left(\frac{M}{LT^2}\right)^{\alpha_1} \times L^{\alpha_2} \times \left(\frac{L^3 M}{T^2 A}\right)^{\alpha_3} \times \left(\frac{LM}{T^2 A^2}\right)^{\alpha_4},$$

and determine the exponents α_j is such a way that the exponents of *mass*, of *time*, of *length* and of *current* are each equal to
zero. Evidently this requires $\alpha_1 = \alpha_4$, $\alpha_2 = 6\alpha_4$ and $\alpha_3 = -2\alpha_4$. We arrive at the combination of parameters

$$\left(\frac{n\overline{M}U^2 R^6 \mu_0}{(\mu_0 Q)^2}\right)^{\alpha_4} = 1. \tag{B1}$$

Choosing $\alpha_4 = 1$ we arrive at the result found in (1), apart from a numerical constant that can not be recovered by dimensional
450 analysis. The parameter combination in (1) is thus the only possible one for the stationary problem.

The dynamic problem is somewhat more complicated. Here we retain also the two last columns in the dimension matrix,
and note that any dimensionally correct combination of parameters can be multiplied by the left side of e.g. (B1), or by
$(n\overline{M}U^2 T_0^2 R^{-1}(\rho D)^{-1})^{\alpha_0}$ to an arbitrary power α_0. We can thus decide that some parameters are kept constant, and determine
the dimensionally correct combination of the rest. To derive a characteristic period of oscillation T_0 we first note that by

Newton's second law $\rho D d^2\Delta/dt^2 = Force$ for the displacement Δ of the magnetopause, we expect the product $\rho D T_0^{-2}$ to appear, rather than these quantities individually. As long as the solar wind pressure is kept constant the variation of the force with varying displacement Δ will be due to the variations of the magnetic pressure with varying distance. We ignore the first column. From the dimension matrix we then have

$$L^{\alpha_1} \times \left(\frac{L^3 M}{T^2 A}\right)^{\alpha_2} \times \left(\frac{LM}{T^2 A^2}\right)^{\alpha_3} \times \left(\frac{M}{L^2 T^2}\right)^{\alpha_4}.$$

We find $\alpha_1 = 7\alpha_4$, $\alpha_2 = -2\alpha_4$, $\alpha_3 = \alpha_4$, giving

$$\left(R^7 \frac{\mu_0}{\mu_0^2 Q^2} \frac{\rho D}{T_0^2}\right)^{\alpha_4} = 1.$$

Taking again $\alpha_4 = 1$, this result is consistent with (3) apart from a numerical factor.

A damping factor arises by a phase difference between the magnetopause displacement Δ and the velocity $d\Delta/dt$, where it is taken into account that it is the relative velocity between the solar wind and $d\Delta/dt$ that matters. A dimensional analysis of this problem will be lengthy.

455 **Appendix C: Radiation belt details**

In this appendix we summarize some details concerning the radiation belt heating due to the asymmetric compression caused by the motion of the Chapman-Ferraro current system. We model the basic averaged gyrocenter velocities by the ∇B-drifts

$$\overline{\mathbf{U}}_{\nabla B} = -\frac{M U_\perp^2}{2q} \frac{\nabla B \times \mathbf{B}}{B^2}, \tag{C1}$$

and curvature drifts (*Chen*, 2016)

460 $$\overline{\mathbf{U}}_{cu} = \frac{M U_\parallel^2}{q} \frac{\boldsymbol{\kappa} \times \mathbf{B}}{B^2 \kappa^2}, \tag{C2}$$

where κ is the radius of curvature for the magnetic field line. Using a magnetic dipole as an approximation we have the expression for a magnetic field line in spherical coordinates as $r = r_0 \sin^2\theta$, where r_0 specifies the reference position on the selected magnetic field line as the distance from the dipole center measured at magnetic equator, $\theta = \pi/2$. The radius of curvature can then be found by standard expressions (*Pécseli*, 2012) as illustrated in Fig. C1. The figure shows the range of
465 validity of (C2) if we assume κ to be constant.

The time T to circle Earth with the combination of the gradient drift and curvature drifts depends on the selected radius and the particle energy. For a 1 MeV particle at a distance of $5R_E$ it takes approximately 10^3 s, or ~ 15 minutes. Combining the velocities in (C1) and (C2) to $\overline{U}$ we have $T = 2\pi r/\overline{U} \sim 1/r\mathcal{W}$ at some distance r from the magnetic dipole center in the magnetic equator plane with $\mathcal{W}$ being the particle energy.

470 **Appendix D: Currents induced in the ionosphere**

The space-time varying electric and magnetic fields generated by the dynamic variations in the position and intensity of the Chapman-Ferraro current system induces currents in the Earth's near ionosphere. The ionosphere has a significant altitude
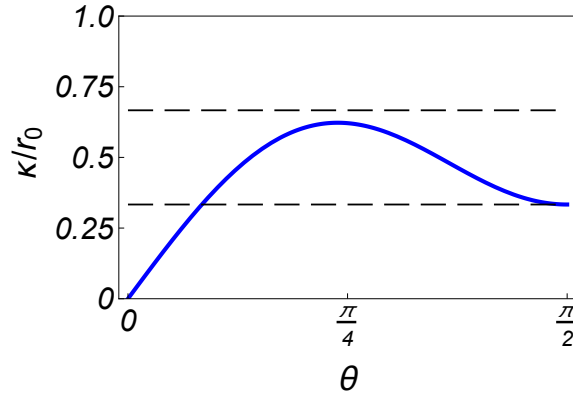
Figure C1. *The variation of the normalized radius of curvature κ/r_0 found as we follow a magnetic field-line specified by r_0, which is the maximum distance it reaches from the Earth's center. Two thin dashed lines give $\kappa/r_0 = 1/3$ and $\kappa/r_0 = 2/3$ for reference. Here θ measures the angle from the magnetic pole.*

variation in the Pedersen and Hall resistivities as well as in the magnetic field aligned conductivity. The problem can be solved only by considering strongly idealized conditions, but these can be helpful by giving insight into some general features.

475 For conditions with large plasma parameters, we have a high plasma conductivity ξ, but it will never be super-conducting conditions, so it will be penetrated by a steady magnetic field. For dynamic conditions with large magnetic Reynolds number $U\mathcal{L}/\xi$ where $\mathcal{L}$ is a characteristic scale size and U a characteristic velocity, we can assume that the ionosphere acts passively for time-stationary magnetic conditions, but responds as an ideally conducting "shell" to rapid temporal changes in electric and magnetic fields. This limit has an exact analytical solution when we assume that the moving image dipole field imposes a

480 locally homogeneous time varying magnetic field at the Earth. In this case we can formulate the question as: "what secondary image dipole is needed to make the boundary conditions at the conducting shell to be fulfilled?", the boundary condition being that the normal component of the magnetic field vanishes at the conducting shell. For the simple limit mentioned before the answer is readily found. We let $B_I(t) = \mu_0 Q_I/2\pi(2R(t))^3$ be the locally homogeneous magnetic field originating from the moving image dipole at a distance of $2R(t)$ from the Earth, see Figs. 1 and 3. We now introduce one more image magnetic

485 dipole with dipole moment $\mathbf{Q}_S$ placed at the Earth's center. For the radial and angular variations of the total magnetic field we have

$$B_r = \left(B_I - \frac{\mu_0 Q_S}{2\pi r^3} \right) \sin\lambda \tag{D1}$$

$$B_\theta = \left(B_I + \frac{\mu_0 Q_S}{2\pi r^3} \right) \cos\lambda, \tag{D2}$$

where it is also here most convenient to measure the angle λ from the equator of the dipole. With the given choice of po-

490 larities we find from (D1) that the normal component of the magnetic field at the conducting shell with radius R_E vanishes for $Q_S(t) = 2\pi B_I(t)R_E^3/\mu_0$. At $r = R_E$ we then find from (D2) the angular magnetic field component $B_\theta(t) = 2B_I(t)\cos\lambda$. The corresponding surface current density at the bottom of the ionosphere is then $K_S(t) = 2(B_I(t)/\mu_0)\cos\lambda$ in the direction

perpendicular to $\mathbf{Q}_S$ in the azimuthal direction thus contributing to the electrojet current. From Fig. 4 we note that the assumption of a locally homogeneous magnetic field imposed by the image dipole representing the Chapman-Ferraro current system

495 can be questioned when the magnetosphere is strongly compressed. In such a case we can obtain a slight improvement of the previous result by displacing the image dipole $\mathbf{Q}_S$ slightly in the sun-ward direction. An illustrative result is shown in Fig. D1. An ideally conducting ionosphere would thus shield ground stations completely from temporal variations of the magnetic field. It seems a safe conclusion that a *partially* conducting ionosphere will reduce the effects of the electric and magnetic field variations as detected on ground. The salty waters of the oceans also act as a conductor, albeit poor in comparison to the ionosphere.

500 The time varying electric fields will induce currents also in the oceans, and the resulting (weak) magnetic field variations might be detectable by ground stations.
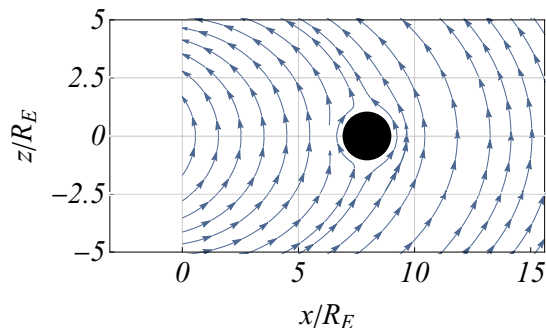
Figure D1. *Illustration of the change in the magnetic field in the vicinity of the Earth in response to a change in the Chapman-Ferraro current assuming an ideally conducting ionosphere. The figure shows only the time-varying part of the magnetic field: the Earth's steady state magnetic field is not included.*

The time variation of the magnetic field at $r > R_E$ follows the variation in $B_I(t)$ directly within the given model, see Fig. 8.